Research Article Vol. 11, No. 7 / July 2024 / Optica 919

OPTICA

Controlling the spectral persistence of a random laser

Pedro Moronta,[1] Pedro Tartaj,[1] Antonio Consoli,[1,2] Pedro David García,[1] Luis Martín Moreno,[3] and Cefe López[1,*]

[1]Instituto de Ciencia de Materiales de Madrid (ICMM), Consejo Superior de Investigaciones Científicas (CSIC), Calle Sor Juana Inés de la Cruz, 3, 28049 Madrid, Spain
[2]Escuela de Ingeniería de Fuenlabrada (EIF), Universidad Rey Juan Carlos (URJC), Camino del Molino 5, 28942 Fuenlabrada, Madrid, Spain
[3]Instituto de Nanociencia y Materiales de Aragón and Departamento de Física de la Materia Condensada, CSIC-Universidad de Zaragoza, 50009 Zaragoza, Spain
*c.lopez@csic.es

Received 16 January 2024; revised 23 May 2024; accepted 5 June 2024; published 2 July 2024

Random lasers represent a relatively undemanding technology for generating laser radiation that displays unique characteristics of interest in sensing and imaging. Furthermore, they combine the classical laser's nonlinear response with a naturally occurring multimode character and easy fabrication, explaining why they have been recently proposed as ideal elements for complex networks. The typical configuration of a random laser consists of a disordered distribution of scattering centers spatially mixed into the gain medium. When optically pumped, these devices exhibit spectral fluctuations from pulse to pulse or constant spectra, depending on the pumping conditions and sample properties. Here, we show clear experimental evidence of the transition from fluctuating (uncorrelated) to persistent random laser spectra, in devices in which the gain material is spatially separated from the scattering centers. We interpret these two regimes of operation in terms of the number of cavity round trips fitting in the pulse duration. Only if the cavity round-trip time is much smaller than the pulse duration are modes allowed to interact, compete for gain, and build a persisting spectrum. Surprisingly this persistence is achieved if the pumping pulse is long enough for radiation in the cavity to perform some 10 round trips. Coupled-mode theory simulations support the hypothesis. These results suggest an easy yet robust way to control mode stability in random lasers and open the pathway for miniaturized systems, as, for example, signal processing in complex random laser networks.

https://doi.org/10.1364/OPTICA.519171

1. INTRODUCTION

Lasers have been a fundamental tool in numerous scientific and technological applications for several decades. These devices, which generate coherent light through a process of stimulated emission, have traditionally relied on the highly precise fabrication of cavities. New laser cavity geometries and unconventional feedback mechanisms are proposed and developed on a regular basis [1]. Some of these new advances are aimed at the fine control over spatial coherence and the number of lasing modes [2]. Already during the late 1960s a laser based on light diffusion was theoretically proposed by Letokhov [3]. The fruit of this disruptive technology (later coined random laser) was experimentally confirmed and the underlying theoretical model refined to include interference [4]. Random lasers (RLs) operate without a well-defined optical cavity, which radically simplifies the process of fabrication and facilitates scalability. Furthermore, RLs show unusual characteristics for a laser (naturally occurring multimode character and low spatial coherence) of interest, for example, in speckle-free full-field imaging [5].

Interest in the use of lasers as nonlinear elements in neuromorphic computing has unsurprisingly grown in the last few years [6]. Artificial neural networks basically consist of an array of a large number of nonlinear nodes (neurons) capable to establish synaptic connections [7]. The intrinsically nonlinear response of laser elements helps to design architectures that favor the interaction in complex networks [8]. For example, vertical-cavity surface-emitting lasers are considered highly promising as building blocks for probabilistic neural network based hardware [9]. Recently, random lasing in complex networks has shown efficient lasing over more than 50 localized modes [10,11]. Also recently, an alternative configuration for random lasers, in which the gain element is separated from the scattering centers, has been proposed as ideal nonlinear elements in photonic neural networks [12]. An advantage of this technology is the scalability and potential integration with stablished technology [13].

The typical RL configuration consists of a disordered distribution of scattering centers in a gain medium under pulsed pumping. This open configuration is inherently prone to spectral and spatial fluctuations and, in fact, under certain conditions,

these fluctuations have been described in terms of the Parisi overlap function (non-trivial equilibrium properties of disordered systems) [14,15]. Such kinds of fluctuations are associated with the intrinsic disorder of RLs that triggers frustration and should not be mistaken for chaotic behavior where equal response is always elicited by equal stimuli. Spectral and spatial fluctuations from pulse-to-pulse in optically pumped RLs have been observed with different active and scattering materials and pumping conditions [16–22]. While fluctuations in RLs have been exploited for specific applications, e.g., spectral super-resolution microscopy [23], they are detrimental in applications that require a high degree of repeatability for synchronization, such as some artificial neural networks. Another large body of research has demonstrated spectral persistence whereby emission of RLs is persistent pulse after pulse. Thus stable emission with persistent frequency peak positions has been predicted in Anderson localized structures, in which modes are tightly localized having limited mutual interaction and competition that prevents spectral fluctuations [24].

Persistent spectral signatures from pulse to pulse have been reported from different materials with Anderson localized structures under varying optical pumping conditions, e.g., from dye doped fibers [25] and polymers [26] with sub-nanosecond and nanosecond [27] pump pulses (100 ps, 600 ps, and 6 ns, respectively), from liquid crystal and dye with nanosecond (8 ns) pumping [28], and from InP nanowires [29,30] and InAlGaAs quantum wells [31] with femtosecond pumping (300 fs and 160 fs, respectively).

Here we show that *spectral persistence* with high correlation in a RL can be achieved both with nanosecond and picosecond pump pulses. We show clear evidence of a transition from a fluctuating (un-correlated successive spectra) RL signal to a persistent spectrum with highly correlated successive spectra even in the picosecond pumping range. Surprisingly, a simple model that considers the distance separating scattering centers and the time it takes for an emitted photon to complete a round trip captures relatively well the existence of this transition. These results suggest an easy yet robust way to control mode interaction stability and open the pathway for rapidly responding miniaturized systems based on RLs.

2. METHODS

A. Sample Preparation

All chemicals were used as received without further purification. Salmon DNA sodium salt, cetyltrimethylammonium (CTMA) chloride, and 4-(dicyanomethylene)-2-methyl- 6-(4-dimethylaminostyryl)-4H-pyran (DCM) were purchased from Sigma-Aldrich.

In a generic procedure, 100 mg of salmon DNA sodium salt dissolved in 20 mL of water (7.5 mM) was added drop by drop to 20 mL of the CTMA chloride aqueous solution (15.8 mM) under magnetic stirring. After 5 h the precipitated DNA-CTMA complex was collected by centrifugation, washed three times with water, and dried at 70°C for 12 h.

Dye-doped DNA-CTMA complexes were prepared by the addition of 0.3 mL of a DCM solution (6.5 mg/mL) in a mixture of ethanol:chloroform (1:1 v/v) to 100 mg of DNA-CTMA dissolved in 1 mL of ethanol-chloroform (6:1 v/v).

The RL devices were prepared by removing the central part of a previously dried drop of TiO2 in a V-shape with a razor blade.

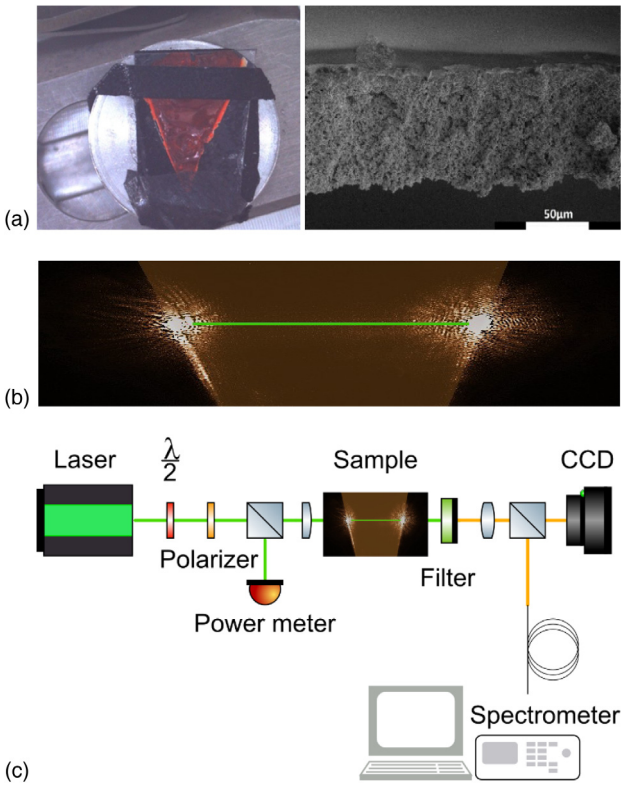

Fig. 1. (a) The sample features a V-shaped design for convenient adjustment of the cavity length without altering other setup parameters as shown in the left photograph of the sample in the holder. The edge is rough as can be seen in the scanning electron microscope image of the cross section on the right. (b) CCD image of a DCM-DNA sample pumped with a 532 nm picosecond laser stripe line. Green line represents the pumping laser area. In operando the sample can be seen as a shining v-shaped area in which two bright spots are formed at the ends of the pumping line (green line). (c) Optical setup scheme to measure spectra and cavity lengths.

The DCM–DNA solution is added to the central part and dried at 70°C. The excess TiO_2 is removed to leave the DNA-DCM with a well-defined V-shape; see Fig. 1(a). TiO_2 is just used to create more roughness on the DCM-DNA edge surface since just cutting the DCM-DNA samples with razor blades creates too smooth a surface.

B. Experimental Setup

Lasing experiments were conducted using two laser systems: a picosecond-pulsed laser (EKSPLA PL2551-B) emitting 30 ps at a repetition rate of 10 Hz pulses and a nanosecond-pulsed laser (LOTIS LS- 2134N) emitting 15 ns pulses at a repetition rate of 5 Hz, both operating at 532 nm. Precise control of energy emission was achieved through the utilization of a rotating half-wave plate and a fixed polarizer. A cylindrical lens was employed to generate a stripe line illumination pattern on the sample, highlighted in Fig. 1(b) with a green line. Emission was collected from the rear of the sample using a 10× microscope objective. The collected emission was then focused using a lens onto a CCD camera and an optical fiber by splitting the beam with a beam splitter.

The optical fiber was connected to an Andor Shamrock 303 spectrometer equipped with an iDus Spectroscopy CCD. A grating with a density of 1799 lines/mm was employed, providing

a resolution of 0.034 nm across a 33 nm spectral window. The spectral acquisition is triggered by each respective Q-switched laser trigger. Another CCD camera within the system was used to measure the average cavity length by capturing images of the sample. To prevent laser pumping emissions from entering the CCD and spectrometer devices, an optical long-pass filter (Thorlabs FEL0550) was positioned in front of the collecting microscope objective.

For precise positioning, a three-axis stage was employed to adjust the height of the pumping position on the sample, while a two-axis stage facilitated horizontal movement of the collecting fiber. The entire setup is shown in Fig. 1(c).

C. Theory

The electromagnetic field can be described as a combination of various modes along with their amplitudes, following the principles outlined in the equations of the coupled mode theory [32]:

$$\frac{da_k}{dt} = i\delta_k a_k - \alpha_k a_k + \sum_{j\neq k} c_{k,j} a_j + g(t,\delta_k)\frac{a_k}{1+\gamma_k|a_k|^2},$$

where $a_k(t)$ is the complex amplitude of the k-th mode; $\delta_k = \omega_k - \omega_0$ with ω_k the angular frequency of the mode and ω_0 the central frequency of the system; dimensionless α_k contain the inverse frequency-normalized ($\alpha^{-1} = \tau\omega_0$) decay times of each mode, $c_{k,j}$ the coupling coefficient with the other modes of the system, $g(t,\delta_k)$ the gain of the active medium, and γ_k the saturation coefficient. All the parameters are scaled by the central frequency ω_0, by letting $\delta_k \to \delta_k/\omega_0$.

For our simulations, we define an arbitrary selection of N_m modes across the spectral bandwidth region ($\Delta\omega = 0.01$). The number of modes, N_m, determines the average frequency spacing $\Delta\omega/N_m$. These modes are utilized to run 100 simulations, wherein the fields of the system, $a_k(t=0)$, are randomly initialized. The losses of these modes are also randomly specified as inverse decay times τ, normally distributed around an average decay time τ_0 set at 0.5 ps with a standard deviation of 0.015 ps.

The gain is defined by an expression that represents the spectral bandwidth of the gain and another temporal expression defining the pulse duration. This temporal profile represents the Gaussian pulsed pump $g(t) = g_0 \exp\left\{-\left(\frac{(t-t_{p0})}{\tau_p}\right)^2\right\}$. The stablished parameters are $t_{p0} = 10^5$ and $g_0 = 1$. The full width at half maximum (FWHM) is set to $\tau_p = 25$ ps. The gain linewidth is approximated by a parabolic profile $g(\delta_k) = 1 - (\delta_k/\delta_g)^2$, where $\delta_g = \Delta\omega/2$ defines the gain bandwidth. The saturation coefficient γ_k is set to one.

The coupling coefficients are defined real and decreasing as a function of the modes' spectral separation, such that for every $k > j$ we have $c_{k,j} \propto c_0(1 - |\omega_j - \omega_k|/q)$ if $|\omega_j - \omega_k| < q$, or $c_{k,j} = 0$ if $|\omega_j - \omega_k| \geq q$. The parameter q enables control over the range of detuning over which couplings are effective, which was set equal to $\Delta\omega$ for our experiments. To ensure energy conservation, we define $c_{k,j} + c_{j,k} = 0$. Their initialization includes the magnitude c_0 and a random sign too.

3. RESULTS AND DISCUSSION

A. Optical

The gain element of our devices consists of a DNA-CTMA polymer matrix [33–35] doped with a fluorophore (4-(dicyanomethylene)-2-methyl-6-(4-dimethylaminostyryl)-4H-pyran, DCM dye). The scattering elements, source of feedback, defining the cavities are the edges of the sample, which are irregular with a roughness length of the order of micrometers. We mold our samples with a V-shaped geometry in order to vary the distance between the scattering edges as shown in Fig. 1(a). Multiple scattering emerges from the index difference between the active medium and surrounding air, providing optical feedback. The samples are optically pumped through a cylindrical lens, obtaining a pumped area 20 μm wide and variable length L_c given by the distance between the scattering edges. Scattered light, visible at the ends of the pumping line in Fig. 1(b), is probed with a microscope objective and sent through a fiber to a spectrometer. Further details can be found in Section 2 along with the optical setup scheme in Fig. 1(c).

In Fig. 2, we show the spectra collected for three cavities with different lengths. The pumping fluence is kept constant well above threshold (440 μJ/mm^2) in all experiments. In this way, just by shifting the sample perpendicularly to the irradiated line, it is possible to change the resonator length while keeping the rest of the parameters fixed.

The insets at the top [Figs. 2(a), 2(c), and 2(e)] each display two single-shot spectra to facilitate a comparison of the fluctuations. For $L_c = 330\pm50$ μm [Fig. 2(a)], fluctuations from pulse to pulse affect the relative intensity of the peaks while their spectral position is almost fixed. For $L_c = 1300\pm50$ μm [Fig. 2(c)], fluctuations become important in the wavelength position as well. In the case of $L_c = 1910\pm50$ μm [Fig. 2(e), the largest cavity] two entirely uncorrelated spectra are displayed. Figures 2(b), 2(d), and 2(f) show spectra resulting from accumulation of 50 single shots. For $L_c = 330$ μm [Fig. 2(d)] the accumulated spectrum is similar to the single-shot spectra, where sharp peaks are observed without a discernible baseline, owing to the high degree of wavelength correlation among the modes. For $L_c = 1300$ μm [Fig. 2(e)] some peaks with a prominent curve beneath them appear, indicating that the similarity with the single-shot spectra starts to fade. For $L_c = 1910$ μm [Fig. 2(f)], we observe a broad and smooth signal with no spikes, indicating the lack of correlation between single shots that averages out the signal, leaving a noisy spectrum similar to the fluorescence background. In this context, the peaks represent the modes that can be amplified, while the baseline corresponds to the uncorrelated modes [36]. We interpret this behavior in terms of the relative magnitude of the pulse duration of the pumping laser, and the round-trip time of modes for a given cavity length.

The time it takes for a photon to go around an optical cavity (round-trip time) is $\tau_{rt} = \frac{2nL_c}{c}$, where n is the refractive index of the medium, L_c the length of the cavity, and c the speed of light in vacuum. The number of round trips a photon in the cavity can perform while the pump laser is ON is then given by $N_{rt} = \tau_p/\tau_{rt}$, where τ_p is the pulse duration. Only during this time, τ_p, is the mode in the cavity amplified since, once the pulse ceases, population inversion decays and gain fades. As demonstrated in [37,38], the dye emission pulse has a similar duration as the pumping pulse, differing from the photoluminescence lifetime (under threshold laser emission).

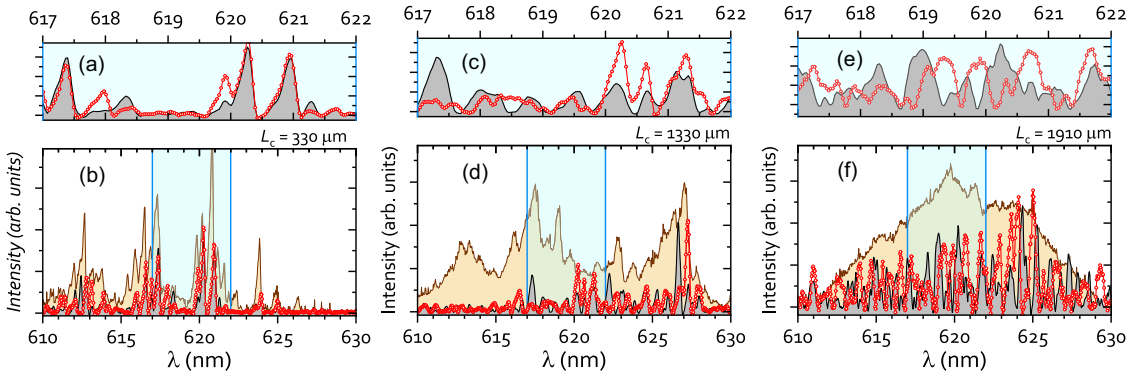

Fig. 2. Typical successive experimental single-shot spectra (gray shaded and red bullets) from RLs with three different cavity lengths: (a) 330 μm, left; (c) 1300 μm, center; and (e) 1910 μm, right panels. Lower panels, (b), (d), and (f) present, on a broader range, the same two successive shots along with the result of accumulating 50 such shots revealing a baseline created when the modes do not exhibit strong persistence through multiple single shots. It is clear that the shortest cavity maintains a more stable spectrum over time compared to the other two, where the modes shift positions and tend to average out. The removal of the baseline was performed to enhance the clarity of wavelength fluctuations.

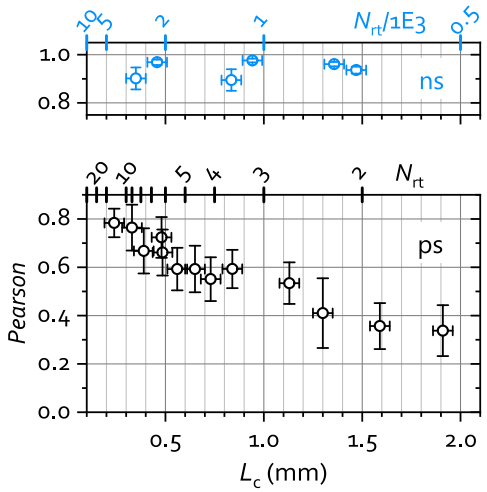

Fig. 3. Pearson coefficient as a function of cavity length. The blue symbols in top panel and black circles in bottom one correspond to the nano- and pico-second regimes, respectively. The top axis scales present number of round trips (in thousands for the nanosecond pumping regime). The Pearson coefficient is the average of 105 pairwise Pearson coefficients obtained from 15 consecutive single-shots spectra.

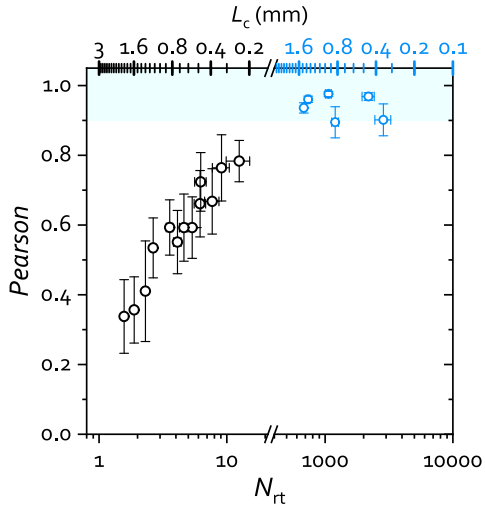

Fig. 4. Pearson coefficient as a function of the number of round trips. The blue and black circles correspond to the nano- and pico-second regimes, respectively. The top axis shows the cavity length in millimeters (in blue for the nanosecond pumping regime). The Pearson coefficient is the average of 105 pairwise Pearson coefficients obtained from 15 consecutive single-shots spectra. The region above 0.9 is shaded to highlight high correlation values.

In our experiment we use a picosecond pulsed laser whose pumping pulse duration is $\tau_p = 30$ ps. For a medium with $n = 1.5$ [39] and a cavity of $L_c = 3$ mm, $\tau_{rt} = 30$ ps $= \tau_p$, a photon would complete one full round trip in the duration of the pulse. The numbers of round trips for $L_c = 330$ μm, 1300 μm, and 1910 μm, the cavities shown in Fig. 2, are around 9.1, 2.3, and 1.5, respectively.

In order to quantify pulse to pulse fluctuations, we employed the Pearson correlation coefficient. This coefficient serves as a measure of similarity between two spectra, with a value of $P = 1$ indicating complete similarity, and $P = 0$ signifying complete dissimilarity. Figure 3 illustrates how the Pearson coefficient changes as a function of cavity length, L_c, approaching a value close to one as the cavity length is shortened. Each data point is obtained by averaging the Pearson coefficient of all 105 pairs of spectra possible between 15 consecutive pump pulses.

The Pearson coefficients obtained with longer pump pulses (≈ 15 ns) are also shown in Fig. 3 (blue dots), to serve as a reference for the most stable cavity. In this case, nanosecond pump measurements exhibit a similar Pearson value for all the cavity lengths that we assign to the number of round trips being always sufficiently large. The same data points are presented as a function of the number of round trips in Fig. 4 to provide a better understanding of the effect we are demonstrating.

It is crucial to emphasize that the Pearson coefficient can potentially lead to incorrect conclusions if the signals are not carefully analyzed. In our context, the mode wavelength is the crucial parameter of interest. The presence of a fluorescence background can artificially inflate Pearson coefficients if baseline signals are not properly removed, causing apparent similarity between signals to arise from the baseline rather than the modes themselves. We applied the *asymmetric least squares smoothing* for baseline correction to all the signals as described in [40] to effectively remove the baseline component from the data. Starting from the five round trips per pulse cavity, a correlation between the modes begins to emerge, with a Pearson index surpassing 0.6. However, it is

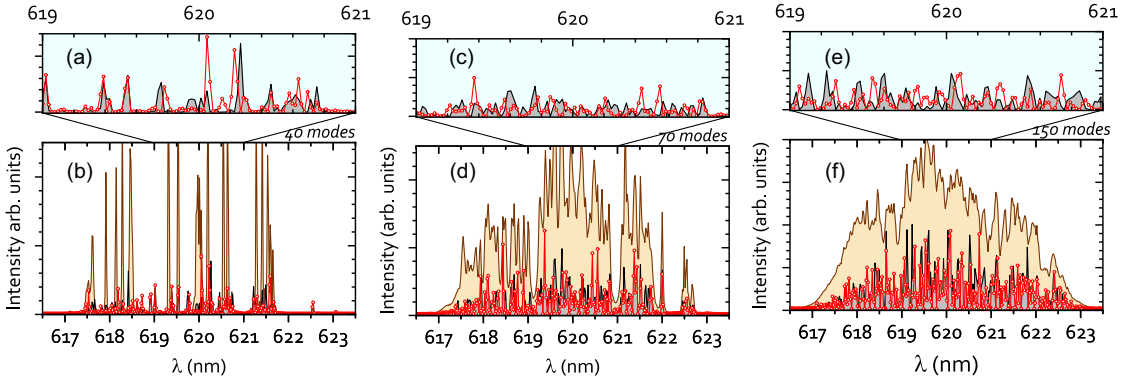

Fig. 5. Typical computed single-shot spectra (gray shaded and red bullets) from coupled mode theory computations with three representative numbers of modes: 40, left; 70, center; and 150, right panels. Lower panels, (b), (d), and (f) present, on a broader range, the same two representative realizations along with the result of accumulating 100 such spectra revealing a baseline created when the modes do not exhibit strong persistence through multiple single shots. It is clear that the resonators with smaller number of modes maintain a more stable spectrum over realizations compared to the other two, where the modes shift positions and tend to average out. Baseline was removed as with the experimental spectra.

from the seven round trips onward that this relationship becomes notably stronger, exceeding the 0.75 threshold. This value is closely aligned with the correlation coefficients observed in the nanosecond domain, where it approaches 0.9. In summary, this suggests that, for this type of sample, achieving an acceptable level of stability within the cavity typically requires around 8 to 10 complete round trips. It is worth noticing that with ns pulses all present cavities offer very persistent spectra and to obtain low correlation values with ns pulses the cavities required would be three orders of magnitude longer (in the meters rather than millimeters range).

B. Numerical Simulation

In order to account for the results observed a dynamical model considering the shape and size of the cavity along with all other physical parameters affecting the lasing action and a complete set of rate equations would be desirable. This is, however, resource and time demanding and a reason for attempting to use a surrogate simpler model. If the hypothesis that the governing parameter that determines the spectral persistence is the round-trip number it is worth considering that we can relate it to the mode spacing. Indeed, $N_{rt} = \frac{\tau_p c}{2nL_c}$, which, using the Fabry–Perot mode spacing, $\frac{\delta\omega}{\omega} = \frac{\Delta\lambda}{\lambda} = \frac{\lambda}{2nL_c}$, can be expressed as $N_{rt} = \frac{\tau_p \delta\omega}{2\pi}$, where $\delta\omega$ is the mode spacing. This puts on an equal footing the number of round trips and the number of modes that can be accommodated in the span of the Fourier transform of the gain time dependence.

We have performed time-CMT calculations with varying numbers of modes randomly spread throughout the gain region (see Section 2). We fix the initial conditions for frequency and gain and provide random seeds for the complex fields, $a_k(t=0)$, in an attempt to simulate the randomness of the spontaneous emission that triggers the lasing action [41]. The computation runs as follows: a set of N_m differential equations with N_m the number of modes is solved yielding $a_k(t)$, $k = 1, \ldots, N_m$, whose sum is Fourier transformed to obtain the spectrum of emission. Each run starts by randomly initializing the $a_k(0)$. Three examples are presented in the lower row of plots in Fig. 5, whose left panel shows two successive spectra (red and black) and the accumulated 100 spectra at the bottom for 40 modes (left); similar results for 70 modes (center), and for 150 modes (right). The top row plots present a zoomed region from the selected ones at the bottom. As

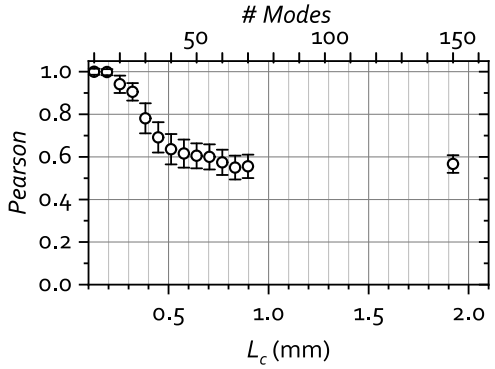

Fig. 6. Pearson coefficient as a function of equivalent cavity length as per the expression $L_c = \lambda^2/2n\Delta\lambda$ for N_m up to 150. The top axis is labeled according to the number of modes of the corresponding Fabry–Perot cavities that fit within the gain range.

can be seen in Fig. 5 increasing the number of modes involved in the calculation, that is, reducing the average spectral separation, leads to more and more dissimilar spectra in successive realization of the random spectra calculation so that the accumulated spectra after many shots grows to be smoother than single spectra and to exhibit a sizable background.

Pearson's correlations between all possible pairs of spectra are computed exactly just as with the experimental results. For each N_m an equivalent cavity length can be assigned assuming a FP mode spacing and the computed correlation as a function of cavity length shows a surprising similarity to that experimentally observed. This can be seen in Fig. 6.

In order to provide a link between the cavity length and the duration of the pump pulse we can consider the following rationale. We have assumed a gaussian pulse in the time domain, $g(t) \approx \exp[-(t/\tau_p)]^2$. Its Fourier transform is also gaussian, $G(\Omega) \approx \exp[-(\Omega/\Delta\Omega)]^2$ with a spread, $\Delta\Omega = 2/\tau_p$ that is inversely proportional to its duration. Using this relation in the expression for the number of round trips, $N_{rt} = \tau_p \delta\omega/2\pi$, we get $N_{rt} = \delta\omega/(\pi\,\Delta\Omega)$. This simple relationship tells that the number of bounces is given by the ratio between the mode spacing of the cavity and the span of Fourier components of the pump pulse. The latter is determined by the cavity length and the former by

the pulse length. Only long enough pulses have narrow frequency distributions compatible with large numbers of round trips.

4. DISCUSSION

We ascribe the observation to the fact that long pulses keep population inversion ON for many round trips so that modes are allowed to interact and compete for gain so that the spectrum generated is consistent with the cavity and its long term or stationary characteristics. However, if the pulse only lasts for a few round trips, modes are not allowed to reach an equilibrium and the spectrum is dominated by the randomness of the spontaneous emission that starts the process and, as a consequence, comes out different after every pulse. It is surprising though that a few return trips along the cavity raise the correlation to values not as high as but near the saturation reached with virtually infinite pulses.

The fact that intense sharp peaks are observed for any cavity length indicates that amplification is always present. However, competition is not effectively established if modes are not allowed sufficient time to couple, exchange energy, and select winners. In addition, it must be remarked that any cavity length of those explored host a sufficient number of modes to produce highly populated spectra. Furthermore, all cavity lengths measured present similar spectral features in terms of peak widths. If we assumed the cavity were a plain 330 μm long Fabry–Perot the mode spacing would be $\Delta\lambda \approx 4 \times 10^{-4}\lambda$ or of the order of 0.34 nm. Such passive laser cavities allow large numbers of modes, and each pump pulse can excite vastly different sets of modes. Only short, in relative terms, cavities allow efficient coupling and competition that lead to persistent spectra.

Synchronization is ubiquitous in nature and a critical element in certain computing schemes [42]. In biological systems, both synchrony and phase relationships between neurons have been proposed to modulate excitation and to guarantee that synaptic activity occurs in a coordinated way [43]. By analogy, we can expect synchronization to take a similar role in an artificial neural network but several orders of magnitude faster than in the brain (nano and picoseconds). Communication in the brain occurs around the millisecond scale associated with the different chemical and electrochemical processes [44]. The millisecond scale, in fact, probably imposes a limitation to the brain size, which may offer insight for the case of a photonic or optoelectronic neural network.

To summarize, in this study we record single-shot spectra from RLs of variable lengths under ps and ns pulsed pumping. We found that under ps pumping only the shorter cavities yield persistent spectra while longer ones present strong variability with different spectra at every pumping event. With this we have demonstrated that it is possible to control the spectral persistence in RLs as revealed by the mutual correlation of successive single-shot spectra. Our experiments have shown that fluctuations in mode behavior between spectra are primarily a result of the fact that the duration of the gain provided by the pumping pulse will not allow sufficient time for mode competition to reach a stationary result when the pulse is too short. In contrast, when the pumping—and subsequently population inversion, hence gain—lasts long enough for photons to resonate in the cavity, stable modes persist. This means that by controlling the number of cavity round trips during a pulse (τ_p/τ_{rt}), we can govern the mode stability of our RLs. In our case, we observe a significant improvement in spectral correlation from pulse to pulse with as few as 10 round trips. This effect is analogous to the transition from an incoherent to a coherent RL. Rather than manipulating the scattering strength, as our sample's edge scatters roughly equally at every point, the variable we modify to change the amplifying path length is the cavity length. Notice that for these effects to manifest under ns pumping the cavity length should be three orders of magnitude longer, in the meter range.

Coupled mode theory simulations where the number of involved modes is used to mimic cavity length dependence of the mode spacing provide support for our findings.

Our research has highlighted the transformation from an unstable random laser to a stable one, featuring intermediate states that facilitate the choice of the optimal configuration for a desired application, or even the ability to fine-tune it within the same device.

Funding. Ministerio de Ciencia e Innovación/Agencia Estatal de Investigación (PDC2022-133418-I00, PID2020-115221GB-C41, PID2021-124814NB-C21); Gobierno de Aragón (ERDF A way of Making Europe, Q-MAD); Comunidad de Madrid (S2018/NMT-4291); Consejo Superior de Investigaciones Científicas (CSIC134E-1794).

Acknowledgment. P.M. acknowledges the FPI contract PRE2019-091452 funded by MICIU/AEI and FSE "invierte en tu futuro." PDC2022-133418-I00 is funded by MICIU/AEI and the EU Next Generation EU/PRTR. PID2020-115221GB-C41 is funded by MICIU/AEI. PID2021-124814NB-C21 is funded by MICIU/AEI and by FEDER UE.

Disclosures. The authors declare no conflicts of interest.

Data availability. The data that support the plots within this paper are available from the corresponding author upon reasonable request. The Python codes developed to execute the calculations presented in this paper are available from the corresponding author upon reasonable request.

REFERENCES

1. H. Cao, R. Chriki, S. Bittner, *et al.*, "Complex lasers with controllable coherence," Nat. Rev. Phys. **1**, 156–168 (2019).
2. M. Nixon, B. Redding, A. A. Friesem, *et al.*, "Efficient method for controlling the spatial coherence of a laser," Opt. Lett. **38**, 3858–3861 (2013).
3. V. S. Letokhov, "Generation of light by a scattering medium with negative resonance absorption," Sov. Phys. JETP **26**, 835–840 (1968).
4. D. S. Wiersma, "The physics and applications of random lasers," Nat. Phys. **4**, 359–367 (2008).
5. B. Redding, M. A. Choma, and H. Cao, "Speckle-free laser imaging using random laser illumination (SI)," Nat. Photonics **6**, 355–359 (2012).
6. B. J. Shastri, A. N. Tait, T. Ferreira de Lima, *et al.*, "Photonics for artificial intelligence and neuromorphic computing," Nat. Photonics **15**, 102–114 (2021).
7. P. R. Prucnal, B. J. Shastri, T. Ferreira de Lima, *et al.*, "Recent progress in semiconductor excitable lasers for photonic spike processing," Adv. Opt. Photonics **8**, 228–299 (2016).
8. A. Consoli, N. Caselli, and C. López, "Networks of random lasers: current perspective and future challenges," Opt. Mater. Express **13**, 1060–1076 (2023).
9. A. Skalli, J. Robertson, D. Owen-Newns, *et al.*, "Photonic neuromorphic computing using vertical cavity semiconductor lasers," Opt. Mater. Express **12**, 2395–2414 (2022).
10. M. Gaio, D. Saxena, J. Bertolotti, *et al.*, "A nanophotonic laser on a graph," Nat. Commun. **10**, 1–7 (2019).
11. D. Saxena, A. Arnaudon, O. Cipolato, *et al.*, "Sensitivity and spectral control of network lasers," Nat. Commun. **13**, 6493 (2022).
12. N. Caselli, A. Consoli, Á. M. Mateos Sánchez, *et al.*, "Networks of mutually coupled random lasers," Optica **8**, 193–201 (2021).
13. A. Consoli, N. Caselli, and C. López, "Electrically driven random lasing from a modified Fabry-Perot laser diode," Nat. Photonics **16**, 219–225 (2022).
14. N. Ghofraniha, I. Viola, F. Di Maria, *et al.*, "Experimental evidence of replica symmetry breaking in random lasers," Nat. Commun. **6**, 6058 (2015).
15. S. Basak, Á. Blanco, and C. López, "Large fluctuations at the lasing threshold of solid- and liquid-state dye lasers," Sci. Rep. **6**, 32134 (2016).

16. G. Zhu, L. Gu, and M. A. Noginov, "Experimental study of instability in a random laser with immobile scatterers," Phys. Rev. A **85**, 043801 (2012).
17. S. Bittner, S. Knitter, S. F. Liew, *et al.*, "Random-laser dynamics with temporally modulated pump," Phys. Rev. A **99**, 013812 (2019).
18. D. Anglos, A. Stassinopoulos, R. N. Das, *et al.*, "Random laser action in organicinorganic nanocomposites," J. Opt. Soc. Am. B **21**, 208–213 (2004).
19. X. H. Wu, A. Yamilov, H. Noh, *et al.*, "Random lasing in closely packed resonant scatterers," J. Opt. Soc. Am. B **21**, 159–167 (2004).
20. K. L. van der Molen, A. P. Mosk, and A. Lagendijk, "Intrinsic intensity fluctuations in random lasers," Phys. Rev. A **74**, 053808 (2006).
21. S. Lepri, S. Cavalieri, G.-L. L. Oppo, *et al.*, "Statistical regimes of random laser fluctuations," Phys. Rev. A **75**, 1–7 (2007).
22. S. Mujumdar, V. Türck, R. Torre, *et al.*, "Chaotic behavior of a random laser with static disorder," Phys. Rev. A **76**, 033807 (2007).
23. A. Boschetti, A. Taschin, P. Bartolini, *et al.*, "Spectral super-resolution spectroscopy using a random laser," Nat. Photonics **14**, 177–182 (2020).
24. P. Stano and P. Jacquod, "Suppression of interactions in multimode random lasers in the Anderson localized regime," Nat. Photonics **7**, 66–71 (2012).
25. B. Abaie, E. Mobini, S. Karbasi, *et al.*, "Random lasing in an Anderson localizing optical fiber," Light Sci. Appl. **6**, e17041 (2017).
26. L. F. Sciuti, L. A. Mercante, D. S. Correa, *et al.*, "Random laser in dye-doped electrospun nanofibers: study of laser mode dynamics via temporal mapping of emission spectra using Pearson's correlation," J. Lumin. **224**, 117281 (2020).
27. A. Sarkar, R. Venkataraj, R. Akshay Krishna, *et al.*, "Silver nanowire mediated random lasing in silica cladded dye doped polymer microstructure," Opt. Commun. **504**, 127466 (2022).
28. Z. Shang, Z. Wang, and G. Dai, "Stability-enhanced emission based on biophotonic crystals in liquid crystal random lasers," Materials-Basel **16**, 200 (2022).
29. M. Rashidi, Z. Li, C. Jagadish, *et al.*, "Controlling the lasing modes in random lasers operating in the Anderson localization regime," Opt. Express **29**, 33548–35557 (2021).
30. M. Rashidi, H. H. Tan, and S. Mokkapati, "Stable, multi-mode lasing in the strong localization regime from InP random nanowire arrays at low temperature," Optica **8**, 1160–1166 (2021).
31. J. Liu, P. D. Garcia, S. Ek, *et al.*, "Random nanolasing in the Anderson localized regime," Nat. Nanotechnol. **9**, 285–289 (2014).
32. H. A. Haus, *Waves and Fields in Optoelectronics*, 1st ed. (Prentice-Hall, 1984).
33. K. Tanaka and Y. Okahata, "A DNA–lipid complex in organic media and formation of an aligned cast film 1," J. Am. Chem. Soc. **118**, 10679–10683 (1996).
34. M. Ibisate, J. F. Galisteo López, V. Esteso, *et al.*, "FRET-mediated amplified spontaneous emission in DNA-CTMA complexes," Adv. Opt. Mater. **1**, 651–656 (2013).
35. M. Leonetti, R. Sapienza, M. Ibisate, *et al.*, "Optical gain in DNA-DCM for lasing in photonic materials," Opt. Lett. **34**, 3764 (2009).
36. S. Mujumdar, M. Ricci, R. Torre, *et al.*, "Amplified extended modes in random lasers," Phys. Rev. Lett. **93**, 053903 (2004).
37. P. Sperber, W. Spangler, B. Meier, *et al.*, "Experimental and theoretical investigation of tunable picosecond pulse generation in longitudinally pumped dye laser generators and amplifiers," Opt. Quantum Electron. **20**, 395–431 (1988).
38. I. Iparraguirre, S. García-Revilla, J. Azkargorta, *et al.*, "Spectro-temporal behavior of dye-based solid-state random lasers under a picosecond pumping regime: Part III," Opt. Express **31**, 7159–7166 (2023).
39. A. J. Steckl, H. Spaeth, H. You, *et al.*, "DNA as an optical material," Opt. Photonics News **22**(7), 34–39 (2011).
40. P. H. C. Eilers and H. F. M. Boelens, *Baseline Correction with Asymmetric Least Squares Smoothing* (2005).
41. M. Leonetti, C. Conti, and C. López, "The mode-locking transition of random lasers," Nat. Photonics **5**, 615–617 (2011).
42. J. Sánchez-Claros, A. Pariz, A. Valizadeh, *et al.*, "Information transmission in delay-coupled neuronal circuits in the presence of a relay population," Front. Syst. Neurosci. **15**, 705371 (2021).
43. P. Fries, "Rhythms for cognition: communication through coherence," Neuron **88**, 220–235 (2015).
44. J. M. Shainline, "Optoelectronic intelligence," Appl. Phys. Lett. **118**, 160501 (2021).